

The three-dimensional swirling flow past a sudden expansion

Gioacchino Cafiero, Giuseppe Ceglia, Stefano Discetti, Andrea Ianiro, Tommaso Astarita and
Gennaro Cardone

Dipartimento di Ingegneria Industriale - Sezione Aerospazio, Università degli studi di Napoli Federico II,
Naples, Italy
stefano.discetti@unina.it

ABSTRACT

The jet flow past an abrupt expansion under some conditions switches intermittently between two states: quasi-axisymmetric expansion and gyroscopic-like precessing motion. In this work an experimental analysis is carried out by means of Tomographic Particle Image Velocimetry (Tomo-PIV). The self-excited flow precession generated by a 5:1 expansion of a round jet in a coaxial cylindrical chamber is investigated. The experiments are performed at a Reynolds number equal to 150,000. Proper Orthogonal Decomposition (POD) is applied to extract information on the organization of the larger structures of the precessing motion. This technique highlights the dominance of three modes: the first two are associated to the jet precession; the third one is representative of the axial motion. Furthermore, an approach based on the modal energy for the evaluation of the precession probability is presented. The application of a stability criterion shows that the self-induced swirl flow results to be unstable within the jet shear layer. The instability is responsible for the generation of helical-shaped vortices in the near field, instead of the expected phenomenology of the ring-vortices generation of circular jets.

1. INTRODUCTION

Considerable attention has been devoted to the development of devices with the aim of exciting and enhancing the large scale coherent structures embedded into the shear layer of turbulent jets. The organization of these structures plays a key role in the transport of mass and momentum in flames [1]. These devices can be bundled in three categories: acoustic excitation (see Reynolds et al [2] for a review), which can be obtained both by external excitation (for example using speakers) or by self-excitation, enjoying the coupling between flow instabilities and acoustic resonance; mechanically oscillating devices [3], effective in cold environment but not well suited for combustion applications, in which the high temperature prevents the use of fast moving parts; fluidically excited devices, like flapping jets [4] or precessing jets [5].

The precessing jet (PJ) device is generated with an axisymmetric jet flowing through a circular nozzle with diameter d and subject to an abrupt expansion in a cylindrical chamber (coaxial with the nozzle) with diameter D and length L . The jet reattaches asymmetrically on the chamber wall after the abrupt expansion, and on the opposite side the fluid is entrained into the chamber from the ambient. Instantaneous asymmetries trigger a rotating pressure field, inducing a precession of the jet, i.e. a rotation of the jet axis around the nozzle axis. The PJ has some analogies with swirl flows, in which, for relatively strong swirl, a precession around the jet axis has been widely documented (the so called precessing vortex core; see Syred [6] for a review).

The description of the phenomenology of the precessing jet is extensively provided in [5]. The flow exhibits an intermittent behaviour, switching between a precessing and an axial mode. In the former the flow field is characterized by a continuously unstable reattaching jet, with a strong recirculation region located on the opposite side of the chamber. A transverse pressure gradient in the outflow is established, thus determining a sharp deflection of the wall jet at the exit of the chamber. Since the flow is in a condition of neutral equilibrium, the effect of any asymmetry and/or the turbulence fluctuations induce the reattachment point to move; as the jet starts to rotate along one direction, the asymmetry of the flow entrained into the chamber induces the establishment of a rotating pressure field. Indeed, the recirculating fluid moves upstream within the chamber and swirls in the opposite direction to that of the precession, thus retaining the net angular momentum equal to zero.

The PJ has shown extremely interesting features in terms of reduction of the global flame strain (thus leading to an increase of the volume of soot). The larger amount of soot enhances the radiative heat transfer, reducing the flame temperature and the production of NOx [7, 8]. PJs have found application in industrial processes in which the radiant heat transfer plays a leading role over convection, such as rotary kilns for the production of cement and lime. Extensive studies have addressed the main statistical features of PJs; however, the investigation of the instantaneous flow field topology is extremely challenging and it is not yet fully characterized, since it is strongly unsteady and three-dimensional. Furthermore, PJs belong to the class of bifurcating flow instabilities arising in symmetrical configuration in absence of initial bias, which are usually difficult to be modelled and numerically simulated [9]. Although PJs have

been used for several applications, there are many aspects of these devices that require a better understanding in order to improve their performances. A clearer knowledge of the flow features development and their dependence on the characteristic parameters that lead the flow would further increase industrial interest in the device.

The parameters that characterize the flow field organization are: fluid properties (density ρ , dynamic viscosity μ), the jet velocity V_j , the jet precession frequency f_p , the nozzle diameter d , the external chamber diameter D and the external chamber length L . According to Buckingham-Pi Theorem [10] the following four non-dimensional groups can be addressed as governing parameters: St_d , Re_d , D/d , L/D , where:

$$St_d = (f_p d)/V_j \quad (1)$$

$$Re_d = (\rho V_j d)/\mu \quad (2)$$

Several studies have concentrated their focus on identifying the best geometric and fluid dynamic conditions to favour jet precession. Nathan et al [5], together with many following works of the same research group [4, 7, 8], focused their interest on the geometry optimization. In most of the cited works the expansion ratio is fixed as $D/d = 5$, which has shown to be very favorable for the precession. The effects of the chamber aspect ratio L/D and of the Reynolds number Re_d on the probability of precession have been widely addressed. Madej et al [11] have shown that the probability of precession is a weakly increasing function of Re_d .

Measuring the Strouhal number associated with the precession St_d and its dependence on the geometric and flow parameters is of fundamental importance as it determines the mixing outside the chamber. Mi and Nathan [12, 13] investigated the influence of the aspect ratio, the inlet geometry and the Reynolds number on St_d . They observed that it increases almost linearly with both the aspect ratio and Re_d . They also demonstrated that the effect of St_d is much more significant than that of Re_d in determining the mixing of the fluids outside the chamber.

In this study an insight into the phenomenology of the fluidic PJs using Tomographic Particle Image Velocimetry (Tomo-PIV) is provided. Very limited attention has been dedicated on the topology of the flow field within the chamber. Furthermore, so far the investigations have been performed with flow visualization [5], phase-averaged measurements with pointwise [15] or planar techniques [11, 16] or with numerical simulations [9, 17]. Tomo-PIV [18], in this sense, can provide a leap forward in understanding the organization of the flow topology in the complicate scenario of an unsteady, intermittent and strongly three-dimensional turbulent flow field; moreover, this technique is well assessed for the study of jet flows [19]. Instantaneous and statistical features are described, providing an insight in the vortices generation and development. A stability analysis of the self-induced swirling flow is also presented. Proper Orthogonal Decomposition is herein used to extract relevant information about the coherent structures of the flow field.

2. EXPERIMENT OUTLINE

2.1 EXPERIMENTAL APPARATUS

The experiments are carried out in a water facility at the University of Naples Federico II. The jet is issued from a circular nozzle (with diameter $d = 20mm$ and length $l = 6d$) installed on the bottom of a nonagonal tank (internal diameter $600mm$, height $700mm$). The jet expands into a cylindrical chamber, coaxial with the nozzle, with diameter $D = 100mm$ and length $L = 275mm$ (so that $D/d = 5$ and $L/D = 2.75$). Both the tank and the cylindrical chamber are made of Plexiglas in order to ensure a full optical access. While in many investigations [12, 13] an exit lip and/or a centre-body have been included into the chamber to favour the precessing motion on the axial one and to condition the exit angle, in this study these arrangements are not considered in order to assess the topology of the flow field without external forcing.

A stabilized water flow rate of $2.3kg/s$ is provided upstream of the nozzle by a centrifugal pump and is laminarized by passing through flow-conditioning grids and honeycombs installed in the plenum chamber. The diameter of the plenum chamber is $5d$ and its length is $20d$, thus no significant effects of fluctuations or bias due to residual swirl are expected in the flow at the outlet of the plenum chamber. In order to check that the effects of asymmetry and bias are negligible, the profiles of the velocity and the turbulent statistics at the exit of the nozzle have been analyzed with planar PIV for the case of outflow without the external chamber. The method implemented by Discetti and Adrian [20] is used to significantly reduce the magnification measurement error. The results reported in Fig. 1 outline that the flow can be reasonably assumed symmetrical and unbiased (in the figure, V represents the axial velocity, $v' = \sqrt{\langle v \cdot v \rangle}$ is the root mean square of the axial velocity fluctuation v , with the angular brackets indicating the operation of ensemble averaging; the quantities are plotted in non-dimensional form using the maximum velocity along the jet axis V_0). The bulk mean velocity V_j of the jet entering the chamber is about $7.5m/s$, thus resulting in $Re_d = \frac{V_j d}{\nu} = 150,000$ where ν is the kinematic viscosity of water equal to about $10^{-6}m^2/s$. For these experimental conditions, the precessing mode is expected to be prevalent on the axial mode; indeed, Madej et al [11] indicated a probability of 65% of precessing motion for $Re_d = 61,900$, $L/D = 2.75$ and $D/d = 5$; besides that, the probability increases with Re_d (although only a weak dependence on Reynolds number is reported in the literature).

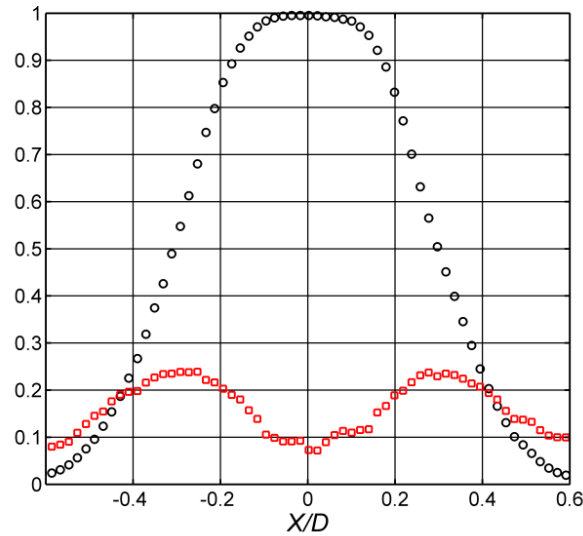


Figure 1 Profiles of the inlet velocity V/V_0 \bullet and of the root mean square of the axial fluctuations v'/V_0 \square without the chamber.

The flow is seeded with neutrally buoyant polyamide particles with average diameter of $56\mu m$, dispersed homogeneously within the facility with a concentration of approximately $0.15\ particles/mm^3$. Laser pulses are produced with a double-cavity Gemini PIV Nd:YAG laser system ($532nm$, $200mJ/pulse$, $5ns$ pulse duration). The exit beam of $5mm$ diameter is shaped into a parallelepiped volume. A knife-edged slit is placed along the laser path to obtain a $y - z$ section of the illuminated volume of $250 \times 34mm$. Four LaVision Imager sCMOS 5.5 Megapixels cameras with identical lenses ($100mm$ EX objectives) in Scheimpflug arrangement are setup on one side of the water facility covering an angle of 90° , as sketched in Fig. 2. The lenses operated with $f_\# = 16$ and since the average magnification in the center of the measurement volume is about 0.06, a depth of field of more than $200mm$, a digital resolution of $10\ voxels/mm$ and a particle diffraction limited minimum image diameter of $3.4\ pixels$ [21] are provided.

Sequences of the tracers particles with time separation of $130\mu s$ are captured at a frequency equal to $10Hz$. This frequency is not sufficient for the sampling of the temporal evolution of the vortical features within the shear layer. Nonetheless, the acquisition frequency is certainly higher than the Nyquist one needed for an appropriate sampling of the precessing motion. In fact, the Nyquist frequency is expected to be about $1\ Hz$ according to the typical values of the Strouhal number St_d reported in the literature of about 0.0015 [12, 13].

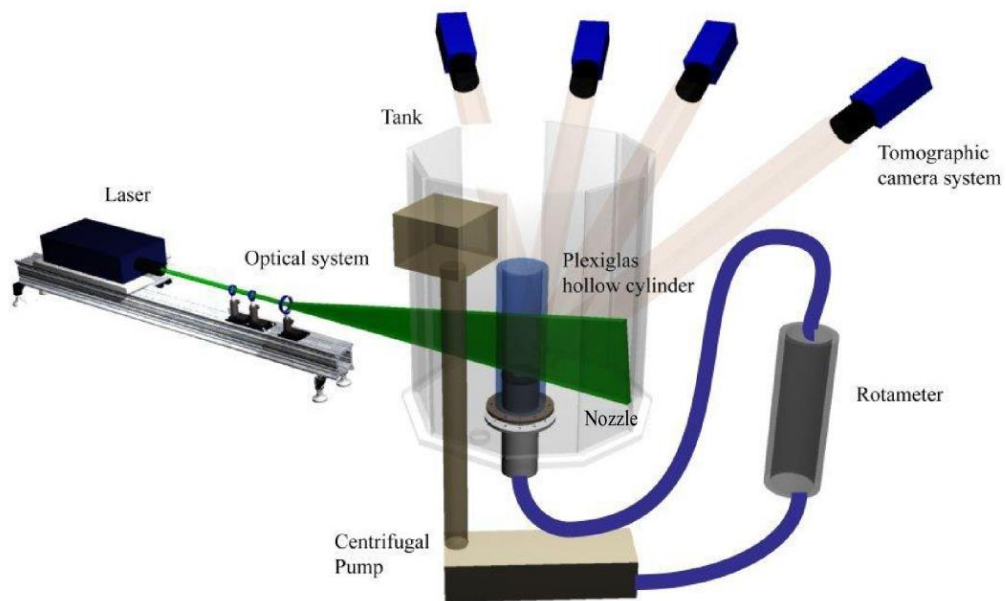


Figure 2 Sketch of the illumination and camera arrangement of the Tomographic PIV system.

2.2 TOMOGRAPHIC PIV: PROCEDURE AND DATA PROCESSING

An optical calibration is performed by recording images of a two levels spatial calibration target (the separation between the levels is $3mm$) mechanically translated along the depth direction of the measurement volume in the range $\pm 20mm$. The calibration markers are white dots on a dark background, equally spaced along two orthogonal directions. A template-matching technique, with a cross-correlation based algorithm, is used to identify the location of the markers. The rms of the initial calibration error is about $0.8 pixels$.

The challenge in the application of this procedure resides in the impossibility to perform the calibration in-situ due to physical restrictions, i.e. the calibration is performed without the presence of the chamber. For this reason the volume self-calibration [22] is the keystone for a successful experiment, as it can correct the mapping functions to account for misalignment of the lines of sight due to refraction effects along the optical path (see, for example, the application in a combustion chamber by Baum et al [23]). The final rms of the calibration error is reduced down to $0.05 pixels$.

The acquisition and the pre-processing of the set of 500 images are performed using LaVision DaVis 8. A measurement volume of $100 \times 250 \times 34 mm^3$ (i.e. $1D \times 2.5D \times 0.34D$) is reconstructed using a custom-made multi resolution algorithm with MLOS initialization, 3 MART iterations on a binned $2x$ configuration and 2 final MART iterations on the final resolution [24]. A further accuracy improvement is obtained by applying a SFIT technique [25] with anisotropic filtering on a $3 \times 3 \times 1$ kernel, with Gaussian distribution of weights and standard deviation equal to 1. The volume is discretized with $10 vox/mm$, thus resulting in a reconstruction volume of $1000 \times 2500 \times 340 voxels$.

The cross-correlation analysis is performed using an algorithm based on direct sparse cross-correlations and redundancy avoidance [26]. The final interrogation spot is $64^3 voxels$ (corresponding to $6.4 \times 6.4 \times 6.4 mm^3$) with 75% overlap (thus resulting in a vector spacing of $1.6mm$). The uncertainty on the velocity measurement can be assessed by applying physical criteria, for example by computing the divergence of the velocity field. The uncertainty in the divergence is both due to the measurement error on the velocity and the numerical truncation in the derivative calculation; however, the 75% overlap reduces this second source of error, thus making it possible to quantify with reasonable approximation the uncertainty on the velocity measurement using the standard deviation of the divergence. Considering the typical value of the vorticity within the shear layer ($0.2 voxels/voxel$) as a reference, for the raw velocity field the standard deviation is $0.028 voxels/voxel$ ($0.14 voxels/voxel$ in the non-dimensional version); the uncertainty is reduced to 0.023 if a low-pass Gaussian filter on a kernel $3 \times 3 \times 3$ and standard deviation equal to 1 is applied.

2.2 PROPER ORTHOGONAL DECOMPOSITION IMPLEMENTATION

The Proper Orthogonal Decomposition (POD) is a powerful technique aimed to extract relevant information about the coherent structures of the flow field. The mathematical procedure identifies an orthonormal basis using functions estimated as solutions of the integral eigenvalue problem known as Fredholm equation (see Sirovich [27] for a more rigorous formulation). Consider for example a function $\underline{U}(\underline{x}, t)$ that is approximated as:

$$\underline{U}(\underline{x}, t) = \langle \underline{U}(\underline{x}, t) \rangle + \underline{u}(\underline{x}, t) = \langle \underline{U}(\underline{x}, t) \rangle + \sum_{n=1}^{Nm} f_n(t) \underline{\varphi}_n(\underline{x}) \quad (3)$$

where \underline{x} and t indicate the spatial and temporal coordinates, respectively. The functions $\underline{\varphi}_n$ constitute the decomposition basis of the fluctuating velocity field and $f_n(t)$ are the time coefficients. The symbol Nm indicates the number of modes used to decompose the velocity field. The solution is not unique since it depends on the chosen basis functions $\underline{\varphi}_n$. The snapshots method proposed by Sirovich [27] assumes that the POD modes are calculated as the eigenmodes of the two-points temporal correlation matrix $\underline{\underline{R}}$:

$$\underline{\underline{R}} \underline{\underline{\varphi}} = \lambda \underline{\underline{\varphi}} \quad (4)$$

where $R_{i,j} = \langle \underline{u}(\underline{x}_i, t) \cdot \underline{u}(\underline{x}_j, t) \rangle$. Since $\underline{\underline{R}}$ is a non-negative Hermitian matrix, it has a complete set of non-negative eigenvalues, whose magnitude indicates the energy contribution of the respective eigenmodes.

3. RESULTS AND DISCUSSION

Here and in the following, unless otherwise stated, the letters U, V, W indicate the velocity components along the width, the height and the depth of the measurement volume (respectively X, Y, Z). The corresponding lower case letters u, v, w refer to the turbulent velocity fluctuations obtained by subtracting the mean velocity components from the instantaneous realizations. In the case of a cylindrical reference frame V_r, V_θ, V_z indicate the components along the radial, azimuthal and axial directions respectively. Finally, the symbols u', v', w' are used to refer to the root mean square (rms) of the

turbulent velocity fluctuations. Generally the results are presented in non-dimensional form, using the bulk jet velocity V_j and the chamber diameter D as a reference.

3.1 MEAN FLOW FEATURES

The mean flow field obtained by averaging a set of 500 images is illustrated in Fig. 3. The iso-surfaces of $V/V_j = 0.999$, of the swirl component of the velocity vector (namely $V_\theta/V_j = 0.2$) and the Turbulent Kinetic Energy (TKE) contour plot are represented. Even if the flow is intermittently switching between the precessing and the axial mode, a net non-zero swirl component is detected in proximity of the nozzle. This indicates that when the precession is triggered the direction of rotation is most likely to persist even after switching for limited periods of time to the axial mode. In fact, the swirl component arises in the shear layer in order to balance the overall angular momentum (i.e. in the opposite direction to that of the precession, in agreement with Dellenback et al [28]). This persistence of the sense of precession (and of the swirl in the near field) is related to the driving force of the precessing motion, i.e. the asymmetry of the entrainment. As the precession is triggered at the beginning of the experiment, the entrained fluid "remembers" its asymmetry also when switching to the axial mode due to the dominance of inertia effects.

The figures 4-5 represent the radial profiles of the mean velocity components and the rms of the turbulent fluctuations for three different streamwise locations ($Y/D = 0, 0.25, 0.5$). The profiles of $\langle W \rangle / V_j$ highlights the presence of a significant swirl induced within the lower region of the chamber as already outlined describing the average field (fig. 3). This effect is much stronger than the rate of entrainment of the jet in the near field, as testified by comparison with the profile of $\langle U \rangle / V_j$, which is characterized by much weaker peaks. This difference is smeared out by diffusion when moving downstream.

At the nozzle exit, a significant intensity of the azimuthal fluctuations (w' / V_j) is observed, comparable to that of the axial fluctuations within the shear layer. By moving downstream the axial fluctuation within the shear layer becomes dominant on the other two components. The gap between azimuthal and radial (u' / V_j) fluctuations decreases along the Y direction; it will be shown in Sec. 3.3 that this effect can be addressed to the pairing of helical vortical structures formed within the shear layer due to instability.

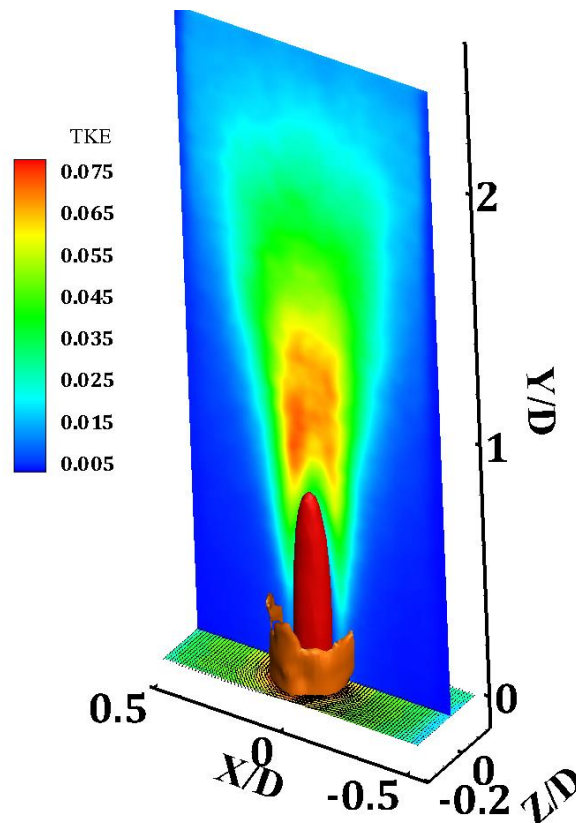


Figure 3 Contour representation of the Turbulent Kinetic Energy on the middle plane of the measurement volume, of the azimuthal velocity on the nozzle exit section, iso-surfaces of $V/V_j = 0.999$ (red) and of $V_\theta/V_j = 0.2$ (light brown)

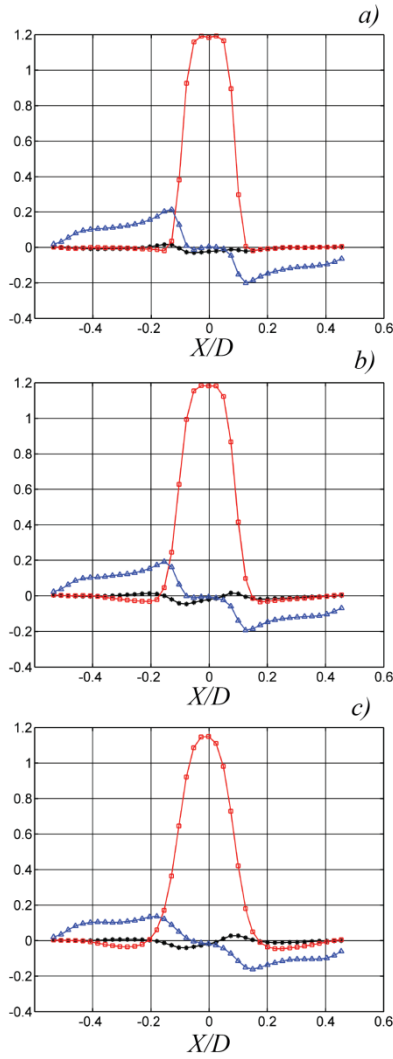


Figure 4 Radial profiles of the mean velocity components for $Y/D = 0, 0.25, 0.5$ (top to bottom). $\star \langle U \rangle / V_j$ $\square \langle V \rangle / V_j$ $\triangle \langle W \rangle / V_j$. Symbols are placed each 2 measured vectors.

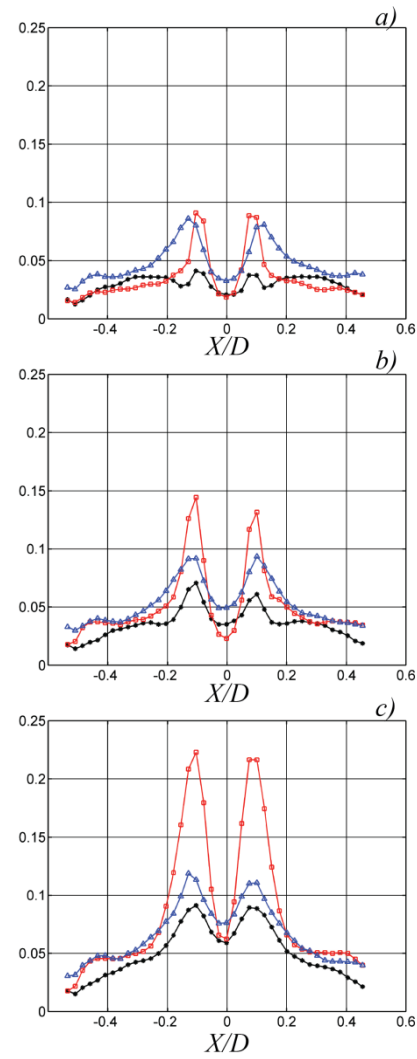


Figure 5 Radial profiles of the rms of the normalized turbulent fluctuations for $Y/D = 0, 0.25, 0.5$ (top to bottom). $\star u' / V_j$ $\square v' / V_j$ $\triangle w' / V_j$. Symbols are placed each 2 measured vectors.

3.2 POD ANALYSIS

The snapshots method (see section 2.3) provides in principle a number of modes equal to the number of snapshots (in this test case, 500 realizations). For clarity, in Fig. 6a the plot is limited only to the first 100 modes, containing about 70% of the energy. The eigenvalues are normalized with respect to their sum, representing the total turbulent energy of the fluctuations. Furthermore, the cumulative sum of the energy is reported in Fig. 6b, in order to assess the number of modes that significantly contribute to build up the decomposition of the velocity field.

The first three modes are reported in Fig. 7, in which the contour representation of the v component normalized with the bulk velocity and the iso-surfaces of $v / V_j = \pm 0.15$ are reported. The first and second modes are associated with the large scale precession, as they present an asymmetric outflow associated with an inflow on the opposite side of the chamber. The difference in the energy pertaining to the first and to the second mode (20.8% and 10.9% respectively, see fig. 6a) is probably related to the geometry of the measurement volume, since it contains the entire inflow and outflow regions for the case of the first mode, while in the second mode the same two highly energetic regions are partly located outside of the observed volume in the far field. The third mode (with 7.5% of energy) is quasi-axisymmetric, as it presents a strong on-axis outflow, associated to the axial mode. As a matter of fact, the ratio of the energy associated to the first two modes and the total energy of the first three modes can be interpreted as an “effective energy–probability” of precessing motion (about 81%). This result is practically in agreement with the measurements of Madej et al (2011); they estimated a probability of the precessing motion of about 61% for $Re_d = 61900$ and $L/D = 2.75$; since the probability of precession increases as Re_d increases, the measured probability value can be considered acceptable.

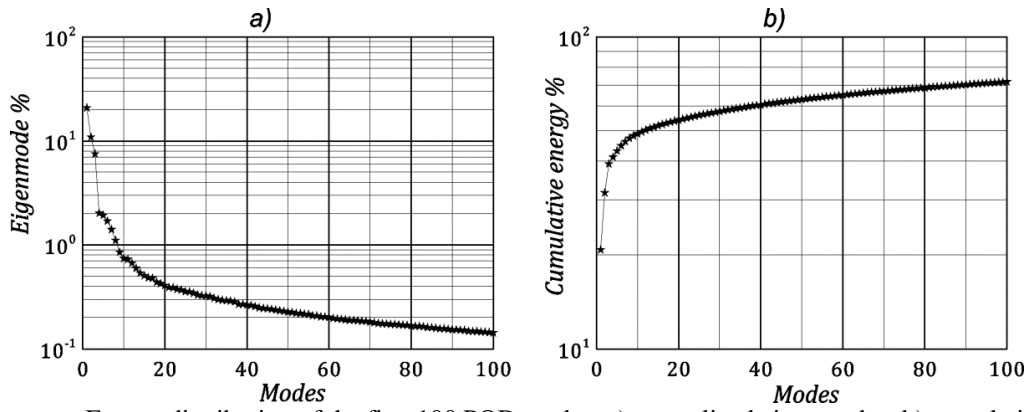


Figure 6 Energy distribution of the first 100 POD modes: a) normalized eigenmodes; b) cumulative energy.

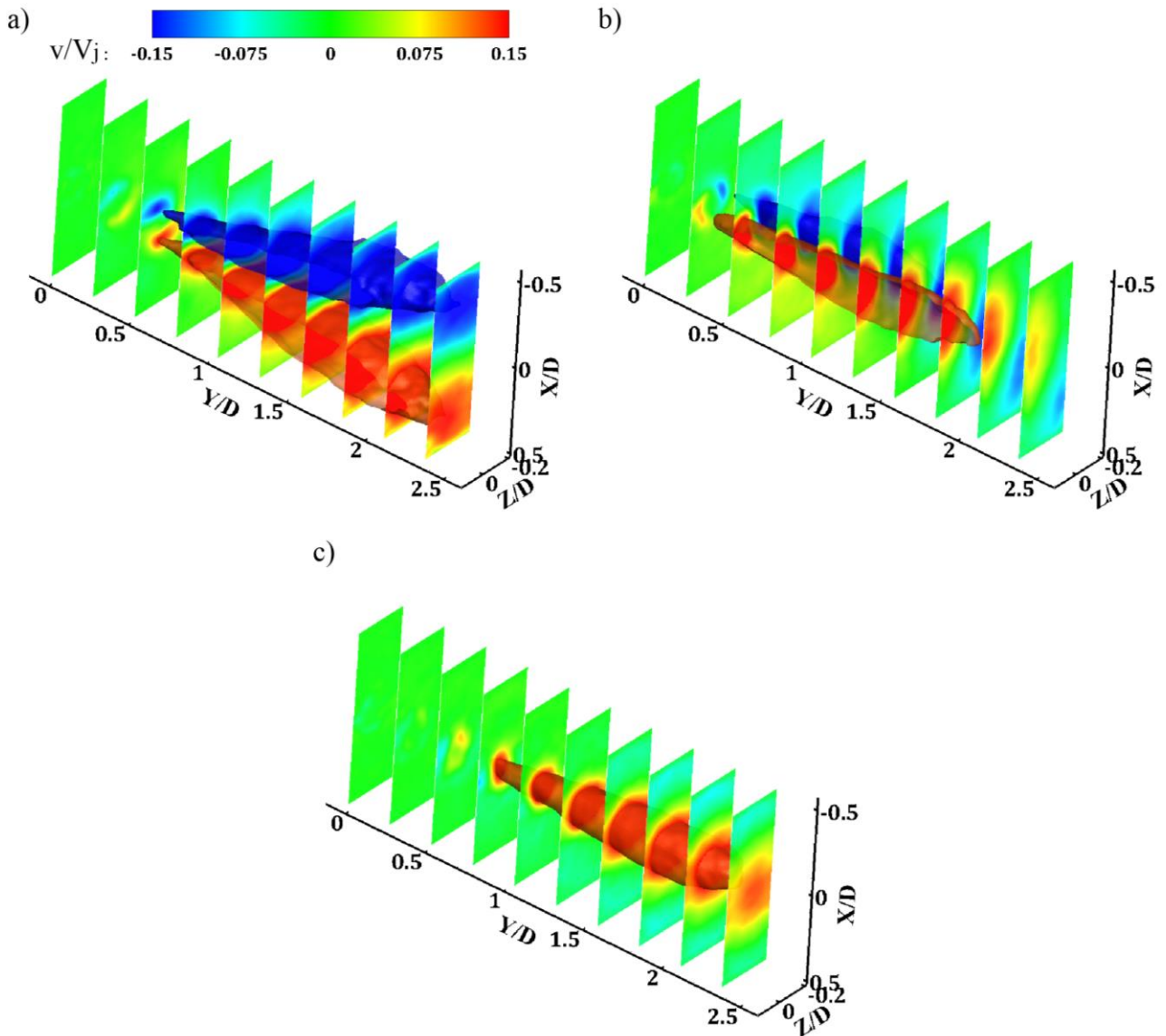


Figure 7 Contour representation on XZ slices of the v/V_j , and iso-surfaces of $v/V_j = 0.15$ (red) and $v/V_j = -0.15$ (blue) for the first (a), second (b) and third (c) POD modes.

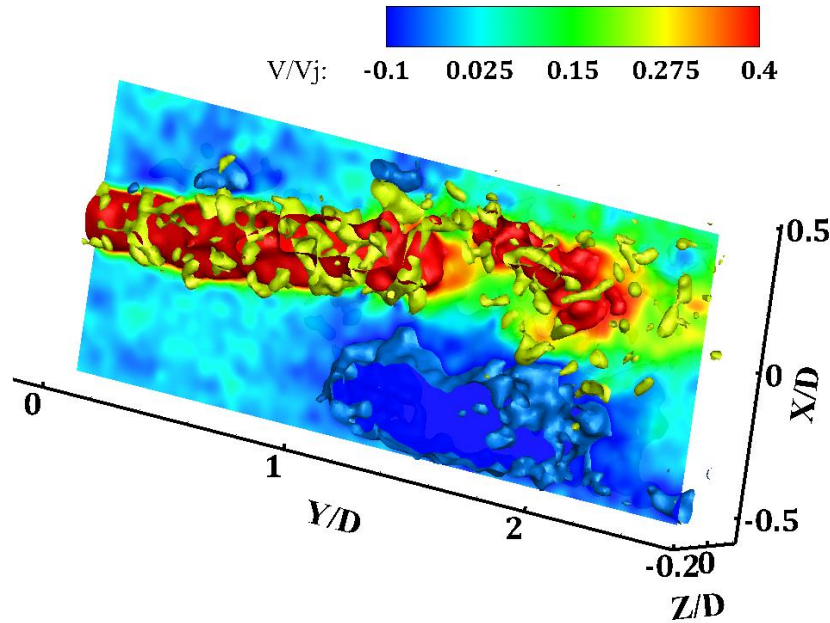


Figure 11 Contour representation of the longitudinal velocity component V/V_j on the middle plane of the measurement volume, and iso-surface of $V/V_j = 0.4$ (red), $V/V_j = -0.1$ (blue) and $Q > 0$ (green).

3.2.1 Instantaneous flow field features

An instantaneous realization of the velocity field for the tested nozzle is shown in Fig. 11. The normalized longitudinal velocity component V/V_j is presented with a contour representation on the middle-plane of the measurement volume along the depth direction; iso-surfaces of $V/V_j = 0.4$, $V/V_j = -0.1$ and $Q > 0$ [29] are also reported.

The jet asymmetrically attaches to the wall and a wide entrainment region is formed on the opposite side to that of impingement. Interestingly enough, the point of attachment is close to $Y/D = 2$, in contrast with the surface visualization reported by Nathan et al [5], reporting the impingement point to be located about at half-height of the chamber. Such a discrepancy is addressed to the presence of the exit lip in the experimental setup by Nathan et al [5], which exasperates the exit angle (and, accordingly, the swirl number of the outlet of the chamber). Consequently the attachment point tends to move upstream due to the stronger induced swirl.

As a consequence of the jet precession, and of the asymmetric recirculation region, an azimuthal velocity component arises in correspondence of the nozzle exit section. This is evident looking at the mean flow field in Fig. 3. Moreover, the self-induced centrifugal motion results to be unstable. Indeed, the Rayleigh stability criterion for an inviscid swirling flow states that a necessary condition for jet instability is [30]:

$$\frac{d}{dr}(V_r^2 r^2) < 0 \quad (5)$$

It has to be noted that, although the considered flow field is viscous, as a matter of fact it can be treated as eulerian for the Reynolds number of the experiment.

Figure 12 shows that the instability condition reported in Eq. (5) is verified within the shear layer at the nozzle exit. The instability generates two helical vortices that can be highlighted in the near field ($0 < Y/D < 0.5$). The absence of the typical ring-vortex phenomenology of circular jets is due to the swirling motion induced by the jet precession. In figure 13 the path of the two helical structures is highlighted with dashed lines. Moving farther from the nozzle exit, these structures tend to merge losing coherence due to the pairing phenomenon [31, 32]. In correspondence of the pairing of the helical structures, the TKE assumes the maximum value, as can be inferred from the average field in Fig. 3.

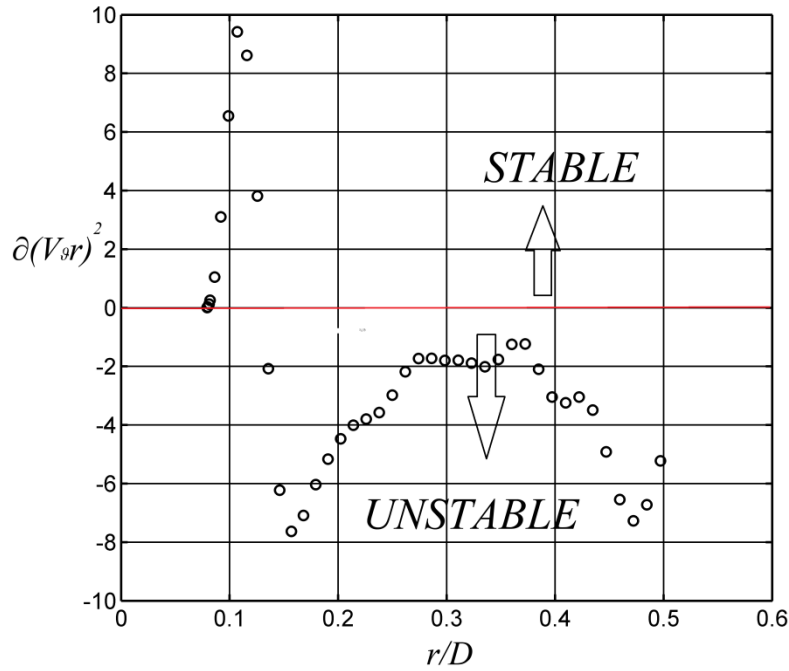


Figure 12 Radial distribution of the Rayleigh stability criterion coefficient.

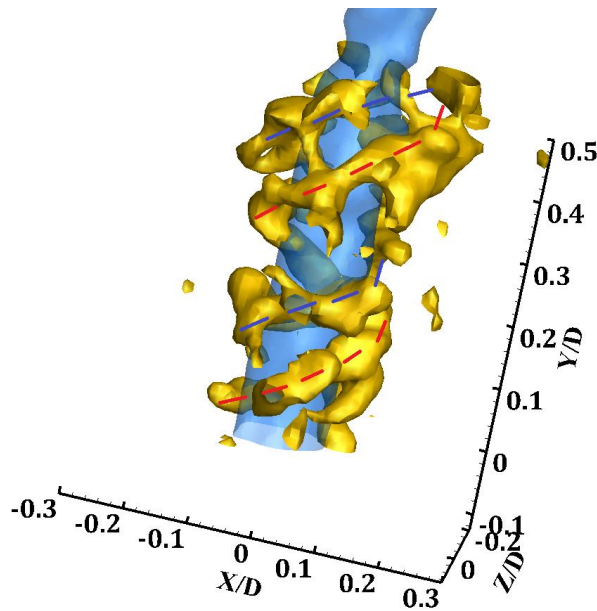


Figure 12 Helical structures identification (red and blue dashed lines). Iso-surfaces for $V/V_j = 0.999$ (blue). Vortical structures are identified using the Q criterion (yellow iso-surface)

4. CONCLUSIONS

The instantaneous and statistical analysis of the flow field leads to the following remarks:

- The driving force of the precession is the inertial effect induced by the asymmetric entrainment (on the opposite side of that of the outflow), triggered by the instantaneous turbulent fluctuations in the condition of neutral equilibrium of the jet attached to the chamber. The entrainment region is extended along the chamber and interacts with an asymmetric recirculation region, placed right below the exiting jet and extending down to the basis of the chamber. The asymmetry of these two regions determines an azimuthal pressure gradient, driving the precession. Furthermore, a swirling motion is imparted to the shear layer of the jet in the direction opposite to that of precession to balance the angular momentum;
- The induced swirling flow results unstable, and generates two helical vortices; these structures evolve for a distance of about $5d$ where the coherence of the structure ceases and the vortices merge according to the pairing phenomenon. Surprisingly enough, the formation of vortex rings due to the Kelvin-

Helmholtz instability does not occur, as it is replaced by the helical vortices. This leads to the conclusion that the precessing jet behaves much more like a swirling jet than a round jet also in the near field.

ACKNOWLEDGEMENTS

The authors kindly acknowledge LaVision GmbH for providing the cameras used in the experiments.

REFERENCES

- [1] Broadwell JE and Mungal MG “Large-scale structures and molecular mixing” *Physics of Fluids A3* (1991) pp. 1193-1206
- [2] Reynolds WC, Parekh DE, Juvet PJD, Lee MJD “Bifurcating and blooming jets” *Annual Review of Fluid Mechanics* 35 (2003) pp. 295-315
- [3] Simmons JM, Platzer MF and Lai JCS “Jet excitation by an oscillating vane” *AIAA Journal* 19 (1981) pp. 673-676
- [4] Mi J, Nathan GJ and Luxton RE “Mixing characteristics of a flapping jet from a self-exciting nozzle” *Flow Turbulence and Combustion* 67 (2001) pp. 1-23
- [5] Nathan GJ, Hill SJ and Luxton RE “An axisymmetric ‘fluidic’ nozzle to generate jet precession” *Journal of Fluid Mechanics* 370 (1998) pp. 347-380
- [6] Syred N “A review of oscillation mechanisms and the role of the precessing vortex core (PVC) in swirl combustion systems” *Progress in Energy and Combustion Science* 32 (2006) pp. 93-161
- [7] Newbold GJR, Nathan GJ, Nobes DS and Turns SR “Measurement and prediction of NO_x emissions from unconfined propane flames from turbulent jet, bluff body, swirl and precessing jet burners” *Symposium (International) on Combustion* 28 (2000) pp. 481-487
- [8] Nathan GJ, Mi J, Alwahabi ZT, Newbold GJR and Nobes DS “Impacts of a jet’s exit flow pattern on mixing combustion performance” *Progress in Energy and Combustion Science* 32 (2006) pp. 469-538
- [9] Guo B, Langrish TAG and Fletcher DF “Numerical simulation of unsteady turbulent flow in axisymmetric sudden expansions” *Journal of Fluids Engineering* 123 (2001) pp. 574-587
- [10] Buckingham E “On Physically Similar Systems: illustration of the use of dimensional equations” *Physical Review* 4 (1914) pp. 345-376.
- [11] Madej AM, Babazadeh H and Nobes DS “The effect of chamber length and Reynolds number on jet precession” *Experiments in Fluids* 51 (2011) pp. 1623-2643
- [12] Mi J and Nathan GJ “Self excited jet-precession Strouhal number and its influence on downstream mixing field” *Journal of Fluids and Structures* 19 (2004) pp. 851-862
- [13] Mi J and Nathan GJ “The effect of inlet flow condition on the frequency of self-excited jet precession” *Journal of Fluids and Structures* 22 (2006) pp. 129-133
- [14] Nathan GJ, Luxton RE and Smart JP “Reduced No_x emissions and enhanced large scale turbulence from a precessing jet burner” *Symposium (International) on Combustion* 24 (1992) pp. 1399-1405
- [15] Wong CY, Nathan GJ and O’Doherty T “The effect of initial conditions on the exit flow from a fluidic precessing jet nozzle” *Experiments in Fluids* 36 (2004) pp. 70-81
- [16] Wong CY, Nathan GJ and Kelso RM “The naturally oscillating flow emerging from a fluidic precessing jet nozzle” *Journal of Fluid Mechanics* 606 (2008) pp. 153-188
- [17] Revuelta A, Sánchez AL and Liñán A “Confined swirling jets with large expansion ratios” *Journal of Fluid Mechanics* 508 (2004) pp. 89-98
- [18] Scarano F “Tomographic PIV: principles and practice” *Measurement Science and Technology* 24 (2013) DOI: 012001
- [19] Violato D, Ianiro A, Cardone G and Scarano F “Three-dimensional vortex dynamics and convective heat transfer in circular and chevron impinging jets” *International Journal of Heat and Fluid Flow* 37 (2012) pp. 22-36
- [20] Discetti S, Adrian RJ “High accuracy measurement of magnification for monocular PIV” *Measurement Science and Technology* 23 (2012) 117001
- [21] Adrian RJ “Particle-imaging techniques for experimental fluid mechanics” *Annual Review of Fluid Mechanics* 23 (1991) pp. 261-304
- [22] Wieneke B “Volume self-calibration for 3D particle image velocimetry” *Experiments in Fluids* 45 (2008) pp. 549-556

- [23] Baum E, Peterson B, Surmann C, Michaelis D, Böhm C and Dreizler A “Investigation of the 3D flow field in an IC engine using tomographic PIV” Proceedings of the Combustion Institute 34 (2013) pp. 2903-2910
- [24] Discetti S and Astarita T “A fast multi-resolution approach to Tomographic PIV” Experiments in Fluids 52 (2012) pp. 765-777
- [25] Discetti S, Natale A and Astarita T “Spatial filtering improved tomographic PIV” Experiments in Fluids 54 (2013) pp. 1505-1517
- [26] Discetti S and Astarita T “Fast 3D PIV with direct sparse cross-correlations” Experiments in Fluids 53 (2012) pp. 1437-1451
- [27] Sirovich L “Turbulence and the dynamics of coherent structures” Quarterly of Applied Mathematics 45 (1987) pp. 561-590
- [28] Dellenback PA, Metzger DE and Neitzel GP “Measurements in turbulent swirling flow through an abrupt axisymmetric expansion” AIAA Journal 26 (1988) pp. 669-681
- [29] Jeong J and Hussain F “On the identification of a vortex” Journal of Fluid Mechanics 285 (1995) pp. 69-94
- [30] Drazin PG “Introduction to hydrodynamic instability” Cambridge texts in Applied Mathematics (2002)
- [31] Winant CD and Browand FK “Vortex pairing: the mechanics of turbulent mixing-layer growth at moderate Reynolds number” Journal of Fluid Mechanics 63 (1974) pp. 237-255
- [32] Yule AJ “Large-scale structure in the mixing layer of a round jet” Journal of Fluid Mechanics 89 (1978) pp. 413-432